

The sedimentation of colloidal nanoparticles in solution and its study using quantitative digital photography

Johanna Midelet¹, Afaf H. El-Sagheer², Tom Brown²,
Antonios G. Kanaras¹, and Martinus H. V. Werts^{*3}

¹University of Southampton, Physics and Astronomy, Faculty of Physical Sciences and Engineering, Southampton SO171BJ, U.K.

²University of Oxford, Department of Chemistry, 12 Mansfield Road, Oxford, OX1 3TA, U.K.

³Ecole normale supérieure de Rennes, CNRS, lab. SATIE, Campus de Ker Lann, F-35170 Bruz, France

February 28, 2017

Abstract

Sedimentation and diffusion are important aspects of the behaviour of colloidal nanoparticles in solution, and merit attention during the synthesis, characterisation and application of nanoparticles. Here we study the sedimentation of nanoparticles quantitatively using digital photography and a simple model based on the Mason-Weaver equation. Quantitative agreement between experimental time-lapse photography and numerical solutions of the model was found for a series of gold nanoparticles. Our method is also relevant for multiparticle assemblies as illustrated by results for DNA-linked dimers. Additionally we derive simple formulas for estimating suitable parameters for the preparative centrifugation of nanoparticle solutions.

*martinus.werts@ens-rennes.fr

1 Introduction

Observations on the sedimentation of colloidal solutions were important historically in establishing the physical reality of molecules and providing a molecular basis for thermodynamics in the form of statistical mechanics.[1–3] Nowadays, there is an intense interest in the development of colloidal solutions of engineered nanocrystals for a variety of applications. These solutions should display sedimentation behaviour in line with expectations for these particles on basis of their shape, composition and suspending medium. For stable and dilute solutions, the sedimentation behaviour (Figure 1) is a result of the particular interplay of nanoparticle hydrodynamics, and gravitational and Brownian forces. Under these conditions, the surface chemistry of the nanoparticles, while ensuring colloidal stability, does not significantly influence the sedimentation behaviour.

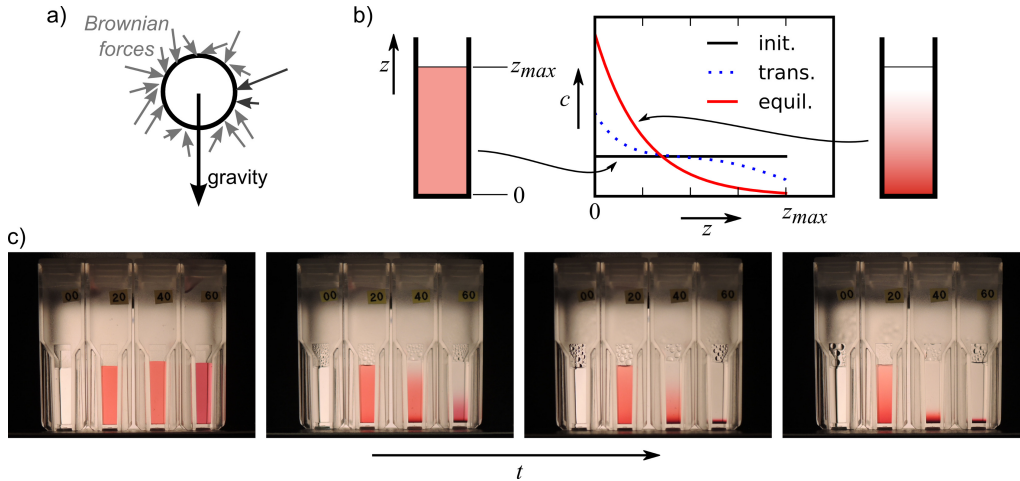


Figure 1 – Sedimentation *versus* Brownian diffusion in colloidal solutions. (a) Gravity tends to direct dense particles to the bottom of the cell, whereas the random Brownian forces tend to disperse the particles over the entire volume. (b) This leads to the establishment of an equilibrium gradient starting from an initial homogeneous distribution of particles. Here we trace the theoretical initial, transient and equilibrium concentration profiles as a function of vertical position. (c) Experimental observation of sedimentation over time of colloidal gold (20, 40, 60 nm) in water using quantitative digital photography. The cell at the left of each picture contains only water. Photos were taken at the start, and after 7, 14 and 35 days, respectively. The rightmost picture represents the cells at equilibrium: a photograph of the Boltzmann distribution.

An understanding of the sedimentation of nanoparticle solutions is useful as it may give rapid, and often visual, clues on the size distribution

and colloidal stability of newly synthesised colloids. These clues go beyond the simple assessment of whether a prepared solution is colloidally stable. Careful monitoring of sedimentation behaviour may be used to verify the nature of the suspended object in its native medium, and is complementary to methods that characterise a limited number of specimens deposited on a substrate, such as electron microscopy. Furthermore, sedimentation, decantation and controlled centrifugation are often a purification step in wet-chemical synthesis of nanoparticles and nanoparticle assemblies, for instance for the purification of gold nanorods.[4] A further example is the purification of nanoparticles by flocculation and subsequent sedimentation. Flocculation under the influence of depletion forces due to specific flocculants produces large aggregates of these nanoparticles that settle rapidly leaving non-flocculated impurities in the supernatant.[5–7].

When analysing the interaction of nanoparticles with biological systems in therapeutic and diagnostic applications, their transport properties such as diffusion and sedimentation need to be taken into account. The importance of sedimentation to *in vitro* studies of cellular uptake of nanoparticles has been demonstrated.[8]

There is a clear connection between the gravitational sedimentation of colloidal particles and analytical ultracentrifugation (AUC), where sedimentation is sped up by increasing g to multiples of the earth gravitational pull. AUC has been successfully applied to the study of nanoparticle solutions.[9–12] Optimisation of the measurement using a spectroscopic approach in combination with detailed numerical analysis of the multi-wavelength sedimentation profiles has made AUC extremely versatile for the analysis of nanoparticle preparations.[13] It has furthermore been demonstrated that information on the shapes of DNA-based nanoparticle assemblies can also be obtained for AUC sedimentation analysis combined with hydrodynamic modeling.[14] A technique closely related to AUC is differential centrifugal sedimentation (DCS) which is based on the sedimentation of injected samples in a spinning disk containing a liquid. DCS successfully detects small changes in particle sedimentation behaviour as a result of their ligand capping,[15] or particle size variations due to varying synthesis conditions.[16]

For these reasons, it is of fundamental interest and instructive to study in greater detail the sedimentation behaviour of nanoparticle solutions. Recently, Alexander *et al.* reported a study of gravitational sedimentation of gold nanoparticles [17]. They focused on measuring the optical density at a pre-defined height in the solution as a function of time using an UV-visible absorption spectrophotometer. This study was then further extended by making estimates of the size distribution of colloidal gold samples by including a multi-wavelength analysis.[18]. Sedimentation has also been instru-

mental for *in situ* attenuated total internal reflection infrared spectroscopy by concentrating the particles or their aggregates onto the substrate.[19]. Magnetic-field enhanced sedimentation of superparamagnetic iron oxide particles has also been investigated.[20]

Here we take advantage of quantitative digital photography[21–23] for experimentally analyzing the time-evolution of the concentration gradient of sedimenting nanoparticle solutions. The technique is simple and easily implemented. When set up properly, time-lapse imaging of the entire nanoparticle concentration gradient is achieved (Figure 1c). In particular with nanoparticles of high overall density (such as those having a golden core) sedimentation may be readily studied without a centrifuge, using the gravitational field alone.

The aim of the present work was to monitor the nanoparticle sedimentation process and the establishment of a concentration gradient using quantitative digital photography, and model this with a simple mathematical diffusion-sedimentation equation. We also discuss the practical implications of the theoretical model for the analysis and purification of nanoparticle assemblies. Furthermore we obtain a photograph of the Boltzmann distribution (rightmost picture of Figure 1c). Whereas this work uses well-known concepts from colloidal chemistry, the emphasis is on the practical application in the purification and characterization of colloidal nanoparticle assemblies.

2 Sedimentation vs diffusion: the Mason-Weaver equation

A simple model for sedimentation can be formulated under the assumptions that there are no interactions between nanoparticles and that their motion is only governed by random Brownian forces and a directional gravitational force. The relevant parameters of the system depend only on the effective density and overall shape of the particles, and on the density, viscosity and temperature of the suspending liquid. The surface chemistry of the particles has no influence, nor does the exact composition of the suspending medium. However, these chemical parameters may influence the model indirectly, *e.g.* by changing density or viscosity of the medium, or by altering particle shape and effective density. We work under conditions where liquid density and viscosity are not significantly altered by the dissolved ingredients, and at low densities of colloid (mass fraction $\ll 1\%$).

The establishment of a concentration gradient in such a dilute colloidal solution of independent, non-interacting particles in a homogeneous gravita-

tional field is described by the Mason-Weaver equation,[24] a one-dimensional partial differential equation. This equation is the direct predecessor to the more well-known Lamm equation[25, 26] that applies for a centrifugal field and which is extensively used in the analysis of ultracentrifuge data.[27]

The height position in the cell is given by z . The concentration of decanting particles c satisfies the Mason-Weaver equation (1), with boundary conditions (2).

$$\frac{\partial c}{\partial t} = D \frac{\partial^2 c}{\partial z^2} + sg \frac{\partial c}{\partial z} \quad (1)$$

$$D \frac{\partial c}{\partial z} + sg c = 0 (z = z_{\max}, z = 0) \quad (2)$$

D is the diffusion coefficient, s sedimentation coefficient, g gravitational constant, and $z = z_{\max}$ and $z = 0$, are the top and bottom of the cell; respectively. In this work, equations (1) and (2) are solved numerically using a Crank-Nicolson finite-difference method which is described in the Supporting Information, Section SI.2. The numerical solver accepts an arbitrary concentration profile as the initial condition.

The initial condition at $t = 0$ that we are interested in is $c = c_0$ for $0 \leq z < z_{\max}$ and $c = 0$ elsewhere. That is, initially the particles are homogeneously distributed within the cell.

The term sg is the terminal velocity of a particle accelerated by gravitational force in a viscous liquid ($v_{\text{term}} = sg$), and represents the velocity (directed towards the bottom of the cell) this particle would have in absence of Brownian motion. It is written in terms of the sedimentation coefficient s . The sedimentation coefficient s for a specific type of particle in a particular viscous liquid is

$$s = \frac{m_b}{f} \quad (3)$$

This involves the *buoyant mass* m_b (*i.e.* the mass of the particle minus the mass of the liquid displaced by the particle) and the *frictional coefficient* f . The frictional coefficient depends on the particle's size and shape and on the viscosity of the solvent (more on this below). The frictional coefficient f also is of importance for the diffusion coefficient D .

$$D = \frac{k_B T}{f} \quad (4)$$

For spherical particles we have the well-known results from Stokes' law and the Einstein-Smolukowski-Sutherland theory given by equations (5) and (6).

Table 1 – Calculated sedimentation parameters and characteristic values for gold nanospheres in water at 277K (4 °C, $\eta = 1.56$ mPa.s). Diffusion (D) and sedimentation (s) coefficients, characteristic height of concentration gradient at equilibrium (z_0), characteristic time for approaching equilibrium from completely dispersed state ($t_{\text{sed}}^{\text{1cm}}$), concentration factor (B^{1cm}). The two latter values refer to a liquid column height of 1 cm. Further data at 298K can be found in the Supporting Information.

diam. nm	D $\mu\text{m}^2\text{s}^{-1}$	s 10^{-9} s	z_0 mm	$t_{\text{sed}}^{\text{1cm}}$ hours	B^{1cm}
13	19.9	0.116	17.556	2450	1.31
20	13.0	0.274	4.821	1030	2.37
40	6.48	1.10	0.603	258	16.6
50	5.18	1.71	0.309	165	32.4
60	4.32	2.47	0.179	115	56.0
80	3.24	4.38	0.075	64.6	133
100	2.59	6.85	0.039	41.3	259
150	1.73	15.4	0.011	18.4	875

$$f_{\text{sphere}} = 6\pi\eta a \quad m_{b,\text{sphere}} = \frac{4}{3}\pi a^3(\rho - \rho_{\text{fl}}) \quad (5)$$

where a is the particle radius, η the viscosity of the liquid, and ρ and ρ_{fl} the mass density of the particle and the suspending fluid, respectively. An underlying assumption of these relation is the non-slip condition at the sphere-liquid interface.

$$s_{\text{sphere}} = \frac{m_b}{6\pi\eta a} = \frac{2}{9} \frac{a^2(\rho - \rho_{\text{fl}})}{\eta} \quad D_{\text{sphere}} = \frac{k_{\text{B}}T}{6\pi\eta a} \quad (6)$$

Table 1 contains diffusion and sedimentation coefficients for gold nanospheres calculated using Eqns. (6) for selected diameters in water at 277K, which is the temperature used in the experiments (see Experimental Details). Data for these particles at 298K can be found in the Supporting Information, Tables SI-2, SI-3, SI-4 and SI-5. The table collects further characteristic values related to sedimentation, which will be discussed below.

At longer times, the solution to the Mason-Weaver equation converges to the concentration distribution at equilibrium, eqn. (7).

$$c(z) = Bc_0 \exp\left(\frac{-z}{z_0}\right) \quad (7)$$

The characteristic height of the equilibrium gradient, z_0 , is

$$z_0 = \frac{D}{sg} \quad (8)$$

Interestingly, by combining (3), (4) and (8), we find that

$$z_0 = \frac{k_B T}{m_b g} \quad (9)$$

The same result for the equilibrium gradient can be obtained using a statistical mechanical approach, *i.e.* calculating the Boltzmann distribution for dense suspended particles in a gravitational field ($E_{\text{particle}} = m_b g z$), illustrating that the digital image of the gold nanoparticle solution at equilibrium is a photograph of a Boltzmann distribution. The concentration profile at equilibrium does not depend on the frictional coefficient nor on the viscosity of the medium, but exclusively on the buoyant mass of the particles. For a spherical particle this translates into

$$z_{0,\text{sphere}} = \frac{3k_B T}{4\pi a^3 (\rho - \rho_{\text{fl}}) g} \quad (10)$$

Some typical values for the characteristic height z_0 for gold nanospheres in water are included in Table 1. For diameters from 13 to 60 nm, the characteristic height falls in the visually interesting 5 cm to 0.2 mm range, and the gradient is readily observed with the naked eye.

Going from the initial dispersed solution to the equilibrium gradient leads to an increase in concentration of the particles near the bottom of the cell. In Eqn. (7) this is expressed in the B constant, which represents the factor by which the particles are concentrated at the bottom. It is obtained by applying mass conservation to Eqn. (7). With initial condition being uniform concentration c_0 throughout the cell ($0 \leq z < z_{\text{max}}$), we obtain eqn. (11). Typical values for gold nanosphere have been added to Table 1.

$$B = \frac{z_{\text{max}}}{z_0 [1 - \exp(-z_{\text{max}}/z_0)]} \quad (11)$$

We found that the time to reach sedimentation equilibrium from the initial homogeneously dispersed state can be estimated to be on the order of the time t_{sed} necessary for a hypothetical particle to traverse the cell all the way from top to bottom (distance z_{max}) at its sedimentation velocity sg .

$$t_{\text{sed}} = \frac{z_{\text{max}}}{sg} \quad (12)$$

Comparison of the numerical solutions for various ratios of z_{max} to sg to the corresponding equilibrium distributions given by Eqn. (7) showed that

the concentration gradient at $t_{\text{equil}} \approx 1.4t_{\text{sed}}$ is in all cases within at few percent of the final equilibrium distribution (see Figure SI-3). This is a useful and hitherto not explicitly stated result. It defines the necessary time window for sedimentation experiments and simulations. In 1 cm high liquid columns, the time needed to reach equilibrium vary from hours to weeks for typical gold nanospheres (Table 1). In practice, with the data analysis demonstrated in this paper, it will not be necessary to run experiments to complete equilibrium, as good estimates for diffusion and sedimentation coefficients can be extracted using the initial progression of the concentration gradient.

3 Experimental details

Temperature stabilisation. In a non-thermostated environment such as a lab shelf, even modest temperature changes may create temperature gradients in the sample that lead to convective motion sufficiently strong to prevent the sedimentation equilibrium from establishing itself. Such convective motion plagued early sedimentation experiments, which were concerned with precise measurement of the equilibrium distribution.[3, 28] Thermally driven convection offers an explanation why on a non-thermostated lab shelf many colloidal gold solutions seem to not to evolve to a sedimentation equilibrium gradient. In the present work, mechanical and thermal perturbations were avoided by carrying out the experiments in a undisturbed laboratory fridge at 277 K.

Quantitative digital photography. In previous work we used quantitative colour imaging for measuring concentration profiles in microfluidic channels, using an optical microscope and a dedicated CCD camera.[29] Here we use a 'consumer-grade' photo camera. Images were taken using a digital camera (Nikon Coolpix P7800, Nikon Corp., Japan) supporting the output of unprocessed ('RAW') image data, where the individual pixel values are proportional to the detected light intensity for the particular colour channel. This circumvents problems of linearization generally encountered with consumer-level digital cameras.[22] Typically, four samples were photographed in a single picture. A black area was also included to serve as the source for background subtraction.

The 'RAW' image data were read into ImageJ software[30] using the dcraw plugin.[31] The three colour channels of the images were separated (ImageJ) and treated individually as monochrome intensity images. Intensity gradient profiles $I_{\text{raw}}(z)$ for all samples (and all colour channels) in each image of the time series were extracted by horizontal averaging over a rectangular

area (typically, the visible optical window of the cells). The pixel values of the black area were averaged for background subtraction, I_{dark} . The z scaling was calibrated by precise measurements of specific cell features. Each image frame thus obtained its specific calibration of pixel size. The digital intensity profiles $I_{\text{raw}}(z)$ were then further treated numerically using the Python programming language with scientific extensions.[32–34]

The individual profile traces with their specific z step sizes were re-sampled at a standard higher resolution in order to have profiles with identical step sizes, which facilitates their processing and comparison with theory. Subsequently, background-corrected image profiles $I(z)$ were obtained by subtraction of the near-zero dark background.

$$I(z) = I_{\text{raw}}(z) - I_{\text{dark}} \quad (13)$$

The top area of each extracted z profile which does not contain liquid was used for calculating the I_0 , by averaging. This corrects for slight frame-to-frame variations in illumination intensity. A linear baseline correction, $\text{OD}_{\text{base}}(z) = k_1 z + k_2$, was applied for each sample globally to all time-frames. In all cases, the baseline correction was only modest and not needed to obtain useful results.

The corrected optical density is finally obtained using eqn. (14). We note that we use this Beer-Lambert-Bouguer formulation despite the condition of monochromatic light not being rigorously fulfilled: the filters used in colour cameras define large spectral bands (width ~ 100 nm). As has been discussed previously,[29] a linear response of the optical density as a function of concentration is still obtained, provided that the extinction spectra of the samples are sufficiently large and their optical density is sufficiently low (under OD 1).

$$\text{OD}(z) = \log_{10} \left(\frac{I_0}{I(z)} \right) - \text{OD}_{\text{base}}(z) \quad (14)$$

Comparison between theory and experiment is achieved by converting the concentration profiles $c(z)$ from the Mason-Weaver model into modeled optical density profiles $\text{OD}_{\text{model}}(z)$ using an "effective extinction coefficient" which we refer here to as k_3 and can be adapted to rescale the model concentration profile to fit the experimental values.

$$\text{OD}_{\text{model}}(z) = k_3 c(z) \quad (15)$$

Centrifugation. A bench-top laboratory centrifuge (Hettich Mikro 220r with 1195-A rotor) was used. Temperature was 298K. The relation between

rotational speed (rounds per minute, RPM) and relative centrifugal force (RCF) is

$$\text{RCF} = 1.12 \times 10^{-3} \times R \times (\text{RPM})^2 \quad (16)$$

The rotor radius R for the 1195-A rotor used is 0.087 m. The maximum speed for this rotor is 18000 RPM, corresponding to an RCF of $31500 \times g$.

Colloidal gold solutions. For the study of the sedimentation of gold nanospheres (Section 4) we used standard aqueous solutions of colloidal gold from commercial sources (BBI Solutions, UK, and Sigma-Aldrich, France) and samples synthesised and characterised according to literature procedures.[35] All colloids are stabilised with negatively charged carboxylate ligands, and the particles have negative zeta potential. The samples were diluted with pure water where necessary. Typical optical densities at the extinction maximum were in the range $0.3 \dots 1$. Under these dilute conditions, the ligands do not influence the sedimentation behaviour of the particles. Also, the only solvent parameters of relevance for sedimentation are the viscosity and the density, and these are very close to those for pure water at low concentrations of stabilising ligand.

DNA-linked dimers. The dimers were constructed from 13 nm gold nanospheres synthesised by the Turkevich method and then submitted to ligand exchange between citrate and *bis*-(*p*-sulfonatophenyl)phenyl phosphine (BSPP) in pure water. After functionalisation of these monomers using single DNA strands (**S1** resp. **S2**), dimers were formed through DNA hybridisation with a third strand **S3**. Click chemistry using azide and alkyne groups on the DNA strands[36] was utilized in order to ensure dimer stability over time. See the Supporting Information, Fig. SI-1 for a schematic, and Table SI-1 for sequences of DNA strands **S1**, **S2** and **S3**.

Gold nanoparticles of diameter 13 nm were synthesised according to the published protocol.[37, 38] Briefly, a solution of sodium tetrachloroaurate (50 mL, 1 mM) was heated up to 100 °C under stirring. Once boiling, a solution of sodium citrate (5 mL, 2 wt.%) was added. After appearance of the typical red colour, boiling and stirring were maintained for 15 additional minutes before letting cool down to room temperature. To stabilise the AuNPs, BSPP was added (15 mg) and the solution was left to stir overnight. TEM images were obtained on a Hitachi H7000 transmission electron microscope operating at a bias voltage of 75 kV. All samples preparation involved deposition and evaporation of a specimen droplet on a carbon film-coated 400 Mesh copper grid. TEM analysis is shown in the Supporting Information, Fig. SI-2.

Dimers of 13 nm AuNPs were synthesised using DNA hybridisation.[36] BSPP-coated AuNPs of 13 nm (5 pmol) were flocculated using NaCl and centrifuged for 5 min at RCF $25\,000 \times g$ (Eppendorf centrifuge 5417R, rotor FA-45-24-11, 8.8 cm radius). The supernatant was taken off and the particles were re-dispersed in 100 μ L buffer (20 mM phosphate, 5 mM NaCl). DNA single strands **S1** respectively **S2** (15 pmol) were added each to a separate nanoparticle solution to achieve a ratio DNA/particles of 3:1. A solution of BSSP (10 μ L, 1 mg/20 μ L) was added and the reaction mixture was shaken for 1 h, in order to deprotect the thiol group on the DNA and to allow its attachment to the particles. The AuNPs were then centrifuged for 15 min at $25\,000 \times g$ and redispersed in hybridization buffer (50 μ L, 6mM phosphate, 80mM NaCl). After mixing the two types of particles (**S1** and **S2** strands), a complementary DNA strand **S3** (2.5 pmol) was added to create the dimers. The hybridisation step was realized by heating up the solution to 70°C and leaving it to cool down slowly and gradually to room temperature. The dimers were purified by agarose gel electrophoresis (1.75% agarose gel in 0.5 x TBE, 1 h at 90V). After extraction from the gel the solution was centrifuged for 10 min at $25\,000 \times g$ and the dimers were redissolved in Milli-Q water. The sample was stored at 4°C.

4 Sedimentation of simple gold nanospheres

Experimental concentration profiles of several settling solutions of gold nanoparticles were obtained from digital photographs taken at different moments. A typical example, using 40 nm gold nanospheres in water, is shown in Figure 2. The photographs for this series (of which 4 are shown in Figure 1) were taken over a 39 day period, and quantitative vertical optical density profiles were obtained using the method detailed in the Experimental section. In this work, we only use the green colour channel of the images, since this produces the strongest optical response for the red-coloured gold nanoparticles.

In the same figure we also show the solution of the Mason-Weaver equation $c(z, t)$ at the same times t . The diffusion and sedimentation coefficients were adjusted independently to obtain best agreement with the experimental observations. The values obtained, $D = 5.1 \times 10^{-12} \text{ m}^2\text{s}^{-1}$ and $s = 7.9 \times 10^{-10} \text{ s}$, agree within 20% with those expected from the Stokes-Einstein and the Stokes relations for perfect 40 nm diameter gold spheres in water at 277 K (Table 1).

Diffusion and sedimentation coefficients were obtained for the entire series of gold nanosphere diameters by fitting the Mason-Weaver solutions to the optical density profiles evolving in time. These coefficients agree reasonably

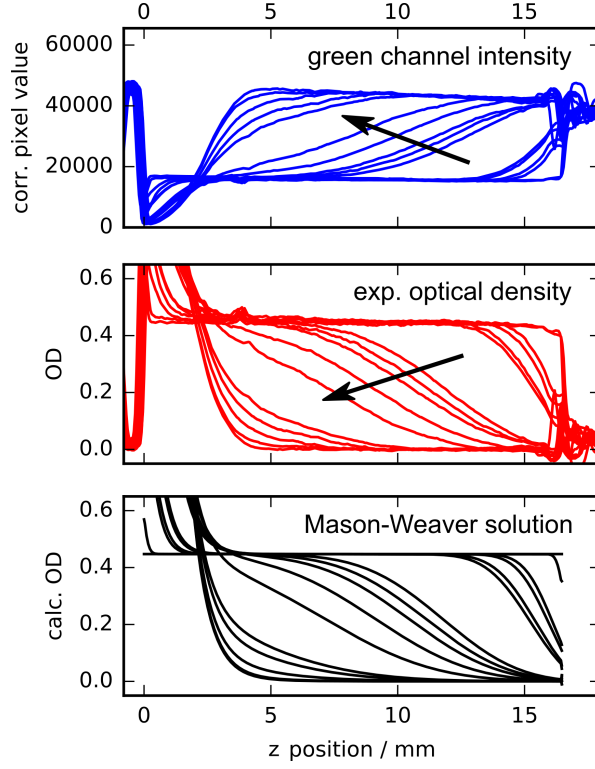


Figure 2 – Evolution of the vertical particle density gradient in aqueous solution of 40 nm diameter gold nanospheres towards sedimentation equilibrium observed using quantitative digital photography at 277K. Photos were taken at $t = 0, 1 \text{ h}, 21 \text{ h}, 27 \text{ h}, 44 \text{ h}, 52 \text{ h}, 7 \text{ d}, 9 \text{ d}, 11 \text{ d}, 14 \text{ d}, 21 \text{ d}, 23 \text{ d}, 28 \text{ d}, 35 \text{ d},$ and 39 days. Top: line-averaged intensities in the green colour channel, corrected for differences in illumination intensity between different images. Middle: experimental optical density profiles obtained from the intensity profiles. The arrow indicates the direction of time. Bottom: theoretical optical density profiles obtained numerically as the solution to the Mason-Weaver equation, with $D = 5.1 \times 10^{-12} \text{ m}^2\text{s}^{-1}$ and $s = 7.9 \times 10^{-10} \text{ s}$.

well (within 20%) with the predicted values (Figure 3). In addition to the predictions based on the gold core only, we also calculated the expected diffusion coefficients for the gold core plus an extra 1 nm of ligand shell ($\rho = 900 \text{ kg m}^{-3}$, dotted curve in Fig. 3). This second theoretical curve demonstrates that the present simple method can not distinguish between small differences in overall hydrodynamic radius and density.

The goals of the present experiment was to verify quantitatively the observations, to confirm the Mason-Weaver equation as a valid model of the behaviour of simple gold nanoparticle solutions, and to obtain an indication of the precision that can be obtained using simple experimental configuration and protocol. Improvements are expected with increased illumination stability and better camera positioning.

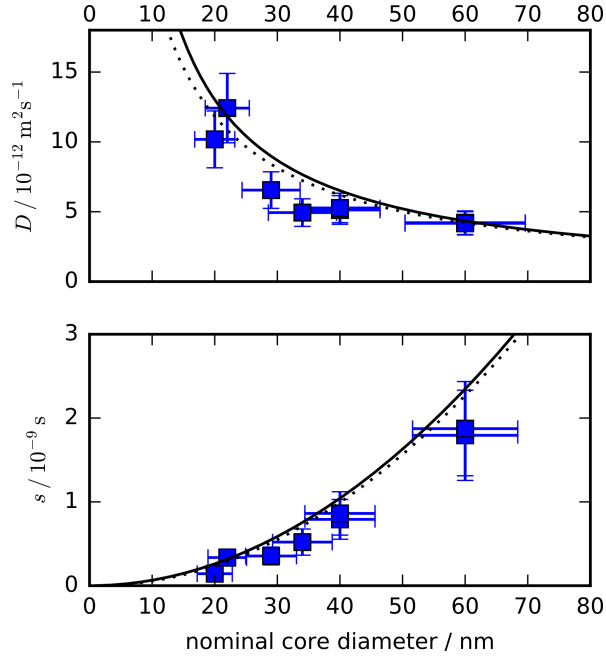


Figure 3 – Diffusion D and sedimentation s coefficients obtained by analysing the evolving experimental density gradient of settling gold nanosphere solutions (square markers). The solid curves are the expected values for perfect golden spheres from the Stokes-Einstein-Sutherland equation (top), and Stokes’ law (bottom). The dotted curves are for gold spheres with a hypothetical 1 nm thick organic layer.

5 Application to nanoparticle assemblies

After the initial demonstration of the quantitative analysis of time-lapse photography of settling spherical gold nanoparticles in water, we investigated a sample of purified DNA-linked dimers of 13 nm diameter gold nanospheres (Figure 4). This experiment is an illustration that studying sedimentation can aid in the chemistry and characterization of biomolecularly-scaffolded multi-nanoparticle assemblies.

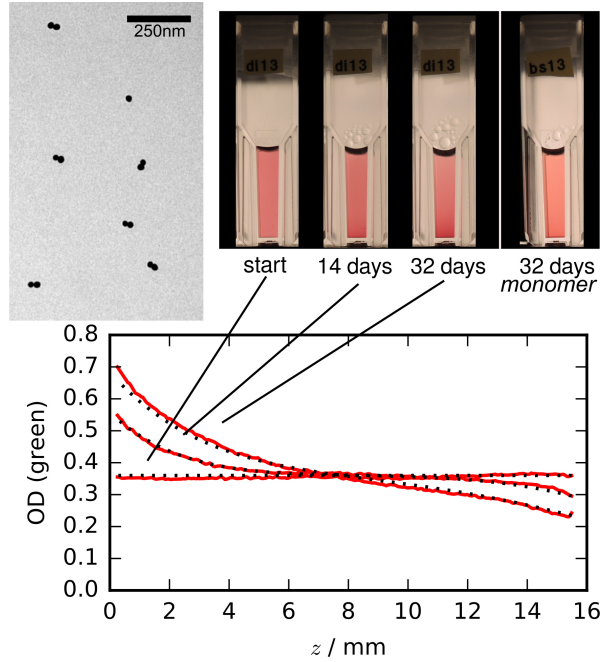


Figure 4 – Top left: transmission electron micrograph of purified DNA-linked dimer sample. Top right: composed image of the time-lapse photography of sedimenting DNA-linked gold nanosphere dimers (at 277 K). The rightmost cell is a sample of monomeric 13 nm gold nanospheres. Bottom: optical density traces as a function of vertical position in the cell, taken at various moments in time (red solid lines); the black dotted curves are the solution to the Mason-Weaver equation with $D = 5.8 \times 10^{-12} \text{ m}^2 \text{ s}^{-1}$ and $s = 9.0 \times 10^{-11} \text{ s}$

Adjusting the curves to the experimental data we obtain $D = 5.8 \times 10^{-12} \text{ m}^2 \text{ s}^{-1}$ and $s = 9.0 \times 10^{-11} \text{ s}$, for the diffusion and sedimentation coefficients, respectively. The sedimentation coefficient of the DNA-linked dimer is slightly smaller than that of a bare 13 nm monomer sphere, *i.e.* it sediments even more slowly. The extra mass from the second gold sphere is counterbalanced by more friction with the solvent due to the larger outer

surface area of the dimer object. The larger volume comes to a large extent from the DNA which has a much lower density than gold.

Additionally, the diffusion coefficient is lower than that of a 13 nm monomer as a result of the larger hydrodynamic volume of the object. For the characteristic height (Eqn. 3) we find $z_0 = 6.6$ nm. This value is close to what we would expect for an object which simply has the double buoyant mass of a 13 nm monomer. This can be explained as follows. Gold has a much higher density than water, whereas the DNA linker has a density comparatively very close to that of water. Any extra volume taken up by the DNA linkage does not significantly contribute to the buoyant mass of the object, since the displaced water volume is replaced with a substance having a density close to that of water. On the other hand, the bulky DNA structure should indeed have an effect on the sedimentation and diffusion constants, *i.e.* sedimentation will be greatly slowed down compared to an equivalent sphere of the same buoyant mass.

The lower sedimentation coefficients leads to slower establishment of the gradient. However, in combination with the lower diffusion coefficient, it finally leads to a more pronounced, shorter density gradient. A further analysis of the hydrodynamic behaviour and the resulting combination of D and s of this type of assemblies is not within the scope of this work, but has received recent attention in the literature.[14]

It is also interesting to note that the estimated time to obtain the final equilibrium gradient (at 277K, with 2 cm liquid height) is on the order of 200 days for both the monomers and the DNA-linked dimers. For analysing the transient concentration profile it is not necessary to wait that long, which demonstrates the interest of having the numerical solution to the Mason-Weaver at hand. Nonetheless, 30 days is still long, and these samples are better analysed with centrifuge-based techniques.[9, 11, 14–16, 39]. In this context, it is interesting to note that — as we will see in the following — the required centrifugal acceleration for many inorganic-core nanoparticles is well within range of standard laboratory centrifuges, instead of higher-speed specialised instruments.

6 Centrifugation of nanoparticle solutions

The results from the Mason-Weaver model may be used to generate approximate initial estimates for preparative and analytical centrifugation. For many nano-assemblies using high-density inorganic core materials, the centrifugal acceleration necessary for rapid sedimentation is well within the capabilities of standard table-top laboratory centrifuges. A centrifugal acceleration that

is much higher than strictly necessary may have deleterious consequences for colloidal stability as the density of nanoparticles in the pellet may become very high, accelerating aggregation. This is one reason why even a rough estimate is of interest. Furthermore, we anticipate that preparative purification protocols may be developed for nanoparticle assemblies by using approximate numerical simulations, using the computer code supplied with the present work.

As an example we consider the minimal centrifugal acceleration g_{cfg} needed to obtain sedimentation equilibrium for gold colloid solutions in a centrifuge within a given time t_{cfg} , *i.e.* our desire is to establish the centrifugal conditions for a typical nanoparticle ‘centrifugation/re-dispersal’ washing procedure. In Section 2 of this paper, we found that the time to reach equilibrium is $1.4t_{\text{sed}}$, and using Eqn. (12) we can roughly estimate the centrifugal acceleration g_{cfg} necessary for the chosen centrifugation time t_{cfg} and a liquid height in the centrifuge tube z_{tube} .

$$g_{\text{cfg}} = \frac{1.4 \times z_{\text{tube}}}{s \times t_{\text{cfg}}} \quad (17)$$

This can be expressed as ‘relative centrifugal force’ (‘times g ’, RCF = g_{cfg}/g , where $g = 9.81 \text{ m s}^{-2}$).

$$\text{RCF} = \frac{1.4 \times z_{\text{tube}}}{g \times s \times t_{\text{cfg}}} \quad (18)$$

Table 2 collects calculated RCF values needed for complete centrifugation of gold colloids in typical Eppendorf-type vials (liquid height $z_{\text{tube}} = 3 \text{ cm}$), within $t_{\text{cfg}} = 30 \text{ min}$. These values were then used in an experiment in which a selection of colloidal gold solutions were spun for 30 minutes at the calculated RCF. The samples were submitted to a typical centrifugation/re-dispersal cycle, in which 95 vol% of the supernatant was removed, followed by redispersal of the (relatively fluid, but highly concentrated) pellet in fresh water. In most cases the recommended centrifugal acceleration worked remarkably well (Supporting Information, Figure SI-5).

Measurement of the UV-visible extinction spectra of the resuspended colloids confirms the visual impression that the calculated RCF values are indeed sufficient, and higher speeds for centrifugation are not necessary. In the case of 20 nm diameter gold spheres, centrifugation at slightly higher acceleration ($\sim 20\%$) was required to concentrate all particles near the bottom of the tube (Figure SI-5).

Centrifugation at a given RCF implies a sedimentation gradient length scale z_0^{cfg} and corresponding concentration factor B_{cfg} . The gradient length should be small enough, such that the nanoparticles are concentrated well in

Table 2 – Calculated RCF values for complete centrifugation, within 30 minutes, of spherical gold nanoparticles in water, using a liquid height of 3 cm. Experimentally determined nanoparticle recovery in a typical centrifugation/re-dispersal washing cycle (n.t. = not tested).

diam. (nm)	calcd. RCF	exp. % recovery
13	11671	n.t.
20	4931	94 (a)
40	1233	n.t.
50	789	98
60	548	n.t.
80	308	97
150	88	97

(a) recovery increases to 97% by spinning at 1.2 times the calculated RCF

the pellet. The concentration factor gives an estimate of the concentration increase at the bottom of the tube. For spherical particles, coefficient s and D for Eqn. (19) are obtained from Eqn. (6).

$$z_0^{\text{cfg}} = \frac{D}{s \times g \times \text{RCF}} \quad B_{\text{cfg}} = \frac{z_{\text{tube}}}{z_0^{\text{cfg}} [1 - \exp(-z_{\text{tube}}/z_0^{\text{cfg}})]} \quad (19)$$

For the conditions in Table 2 z_0^{cfg} decreases from 2.1 μm (for 13 nm diameter gold spheres) to well below 1 μm (larger particles), which indicates that the particles are well concentrated near the bottom of the tube.

Prolonged centrifugation may concentrate smaller particles of less dense materials. If we take for instance particles of 8 nm diameter with average density 4.5 kg m^{-3} in water (a rough estimate for typical[40] CdSe/ZnS quantum dot particles with a small-molecule capping), then it may be anticipated that these can be concentrated in a liquid pellet less than 300 μm high ($z_0^{\text{cfg}} \sim 31 \mu\text{m}$) by spinning them for 6 hours at $11000 \times g$ (or 12 hours at $5500 \times g$ for a $z_0^{\text{cfg}} \sim 63 \mu\text{m}$), starting from a 3 cm liquid height (typical Eppendorf-type vial). Such centrifugation conditions are well in the range of standard laboratory centrifuges.

We may use similar reasoning to find the conditions for minimal centrifugal stress, which will correspond to finding the minimum RCF necessary for a certain pellet compactness (small z_0^{cfg}), and accepting to centrifuge for a prolonged time, given then by t_{cfg} .

Here, we were concerned with centrifugation without density gradient, starting from an initially homogeneous solution. For separation purposes,

density gradient methods may be more adapted.[41] Moreover, we used the Mason-Weaver model which assumes a constant gravitational field, instead of the gradient found in centrifugation. Nevertheless, this simple model does provide a means of predicting the behaviour of nanoparticles in solution in a standard laboratory centrifuge, and is therefore relevant for the rational design of nanoparticle purification protocols.

7 Conclusion

This work rationalises observations on the settling of nanoparticles in liquid solution in the framework of the Mason-Weaver model. It illustrates a quantitative agreement between this model and experimental digital photography for the time-evolution of the concentration gradient of suspended nanoparticles submitted to a gravitational field. A simple experimental protocol is given for observing the sedimentation process in the absence of thermally induced convection using time-lapse digital photography of the samples stored in a undisturbed laboratory fridge.

By fitting a numerical solution of the Mason-Weaver equation to the experimental concentration gradient, the diffusion and sedimentation coefficients D and s are obtained, without necessity to wait for complete equilibrium to be established. Early studies on sedimentation[3, 28] were mostly concerned with precise measurement of the equilibrium gradient, which only yields the buoyant mass m_b of the particle as the sole parameter, not the separate contributions of diffusion and sedimentation coefficients.

We demonstrated that measuring the evolving concentration gradient of settling solutions distinguishes between individual monomeric nanoparticles and their dimeric assemblies, by giving a distinct combination of diffusion and sedimentation coefficients for each type of nano-object.

In our experiments on gold nanospheres in dilute solution, no significant deviations from the simple Mason-Waver model were observed. Colloidal gold solutions are generally known to be well-behaved in this respect, and we expect many dilute solutions of other non-aggregating nanoparticles to behave in a similar way. Any significant deviations from the predictions made by the Mason-Waver model would point in the direction of stronger interparticle interactions, aggregation of individual objects, or changes in the properties of the liquid medium. It is important to be aware of such deviation as they may affect other aspects of the behaviour of the nanoparticles in liquid medium, such as their interaction with biological entities.

Based on the Mason-Weaver model, we obtained simple expressions that give useful recommendations for the centrifugation of nanoparticle solutions,

so that delicate solutions can be processed with care, instead of consistently spinning at maximum RCF.

The simple mathematical model and the experimental protocol used here have obvious limitations, and are no substitute for more advanced analytical centrifugation techniques[9, 11, 14–16, 39]. However, they do provide means for initial and very simple screening of nanoparticle solutions, and rationalise visual observations made at the bench. The practical insights and simple quantitative expressions provided are of direct interest for the wet-chemical synthesis, purification and application of functional nanoparticle assemblies.

Acknowledgements

This work was supported by Dstl (UK) in the framework of the France-UK Ph.D. programme. MW acknowledges funding by the *Agence Nationale de la Recherche* (France), grant ANR-2010-JCJC-1005-1 (COMONSENS).

References

- [1] M. D. Haw. *J. Phys.: Condens. Matter* **2002**, *14*, 33 7769.
- [2] P. Ball. *Chemistry World* **2005**, *2* 38.
- [3] J. Perrin. *J. Phys. Theor. Appl.* **1910**, *9* 5.
- [4] V. Sharma, K. Park, M. Srinivasarao. *Proceedings of the National Academy of Sciences* **2009**, *106*, 13 4981.
- [5] K. Park, H. Koerner, R. A. Vaia. *Nano Lett.* **2010**, *10*, 4 1433.
- [6] L. Scarabelli, M. Coronado-Puchau, J. J. Giner-Casares, J. Langer, L. M. Liz-Marzán. *ACS Nano* **2014**, *8*, 6 5833.
- [7] F. Liebig, R. M. Sarhan, C. Prietzel, A. Reinecke, J. Koetz. *RSC Adv.* **2016**, *6*, 40 33561.
- [8] E. C. Cho, Q. Zhang, Y. Xia. *Nature Nanotechnology* **2011**, *6*, 6 385.
- [9] J. M. Zook, V. Rastogi, R. I. MacCuspie, A. M. Keene, J. Fagan. *ACS Nano* **2011**, *5*, 10 8070.
- [10] R. P. Carney, J. Y. Kim, H. Qian, R. Jin, H. Mehenni, F. Stellacci, O. M. Bakr. *Nature communications* **2011**, *2*, May 335.

- [11] K. L. Planken, H. Cölfen. *Nanoscale* **2010**, *2*, 10 1849.
- [12] B. Demeler, T.-L. Nguyen, G. E. Gorbet, V. Schirf, E. H. Brookes, P. Mulvaney, A. O. El-Ballouli, J. Pan, O. M. Bakr, A. K. Demeler, B. I. Hernandez Uribe, N. Bhattarai, R. L. Whetten. *Anal. Chem.* **2014**, *86*, 15 7688.
- [13] J. Walter, K. Löhr, E. Karabudak, W. Reis, J. Mikhael, W. Peukert, W. Wohlleben, H. Cölfen. *ACS Nano* **2014**, *8*, 9 8871.
- [14] M. J. Urban, I. T. Holder, M. Schmid, V. Fernandez Espin, J. Garcia de la Torre, J. S. Hartig, H. Cölfen. *ACS Nano* **2016**, acsnano.6b01377.
- [15] Ž. Krpetić, A. M. Davidson, M. Volk, R. Lévy, M. Brust, D. L. Cooper. *ACS Nano* **2013**, *7*, 10 8881.
- [16] A. Knauer, A. Thete, S. Li, H. Romanus, A. Csáki, W. Fritzsche, J. M. Köhler. *Chemical Engineering Journal* **2011**, *166*, 3 1164.
- [17] C. M. Alexander, J. C. Dabrowiak, J. Goodisman. *J. Colloid Interface Sci.* **2013**, *396* 53.
- [18] C. M. Alexander, J. Goodisman. *J. Colloid Interface Sci.* **2014**, *418* 103.
- [19] A. I. López-Lorente, M. Sieger, M. Valcárcel, B. Mizaikof. *Anal. Chem.* **2014**, *86* 783.
- [20] V. Prigiobbe, S. Ko, C. Huh, S. L. Bryant. *J. Colloid Interface Sci.* **2015**, *447* 58.
- [21] M. Stevens, C. A. Páraga, I. C. Cuthill, J. C. Partridge, T. S. Troscianko. *Biol. J. Linn. Soc.* **2007**, *90*, 2 211.
- [22] J. E. Garcia, A. G. Dyer, A. D. Greentree, G. Spring, P. A. Wilksch. *PLoS ONE* **2013**, *8*, 11 e79534.
- [23] T. Schwaebel, O. Trapp, U. H. F. Bunz. *Chem. Sci.* **2013**, *4*, 1 273.
- [24] M. Mason, W. Weaver. *Phys. Rev.* **1924**, *23* 412.
- [25] O. Lamm. *Ark. Mat. Astron. Fys.* **1929**, *21B* 1.
- [26] P. H. Brown, P. Schuck. *Computer Physics Communications* **2008**, *178*, 2 105.

- [27] P. Schuck. *Biophys. J.* **2000**, 78, 3 1606.
- [28] N. Johnston, L. G. Howell. *Phys. Rev.* **1930**, 35 274.
- [29] M. H. V. Werts, V. Raimbault, R. Texier-Picard, R. Poizat, O. Français, L. Griscom, J. R. G. Navarro. *Lab. Chip* **2012**, 12 808.
- [30] C. A. Schneider, W. S. Rasband, K. W. Eliceiri. *Nature Methods* **2012**, 9 671.
- [31] D. Coffin. dcraw. URL <http://www.cybercom.net/~coffin/dcraw/>.
- [32] K. J. Millman, M. Aivazis. *Computing in Science & Engineering* **2011**, 13, 2 9.
- [33] S. Van Der Walt, S. C. Colbert, G. Varoquaux. *Computing in Science and Engineering* **2011**, 13, 2 22.
- [34] J. D. Hunter. *Computing in Science and Engineering* **2007**, 9 90.
- [35] N. G. Bastús, J. Comenge, V. Puentes. *Langmuir* **2011**, 27, 17 11098.
- [36] A. Heuer-Jungemann, R. Kirkwood, A. H. El-Sagheer, T. Brown, A. G. Kanaras. *Nanoscale* **2013**, 5, 16 7209.
- [37] J. Turkevich, P. C. Stevenson, J. Hillier. *Discuss. Faraday. Soc* **1951**, 11, c 55.
- [38] J. Turkevich, P. C. Stevenson, J. Hillier. *J. Phys. Chem.* **1953**, 57, 7 670.
- [39] J. B. Falabella, T. J. Cho, D. C. Ripple, V. A. Hackley, M. J. Tarlov. *Langmuir* **2010**, 26, 15 12740.
- [40] A. R. Clapp, E. R. Goldman, H. Mattoussi. *Nat. Protoc.* **2006**, 1, 3 1258.
- [41] B. Kowalczyk, I. Lagzi, B. A. Grzybowski. *Current Opinion in Colloid & Interface Science* **2011**, 16, 2 135.

SI Supporting Information

SI.1 Synthesis of DNA-linked gold nanosphere dimers

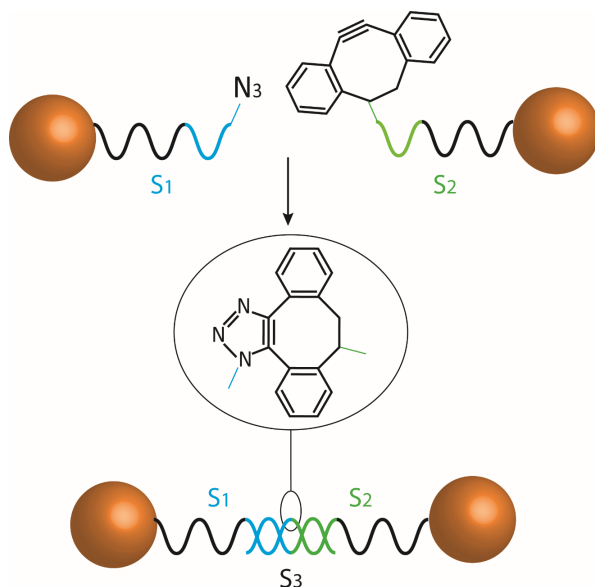


Figure SI-1 – Schematic of the assembly of DNA-linked dimers and subsequent 'click' chemistry.

Table SI-1 – Sequences of single DNA strands **S1**, **S2** and **S3**.

Abbreviation	DNA sequence and modifications
S ₁ (azide derivative X1)	5' – (C ₆ H ₁₂ S)AAAAAAAACGAGTGCTAAGGATCCGAAX1
S ₂ (alkyne derivative X2)	3' – (C ₆ H ₁₂ S)AAAAAAAAGCTTACCTATAGACGTCACCTTX2
S ₃ (Splint)	5' – ACACACCGAATGGATATCTGCAGTGAATTCGGATCCTTAGCACTCGACACAC

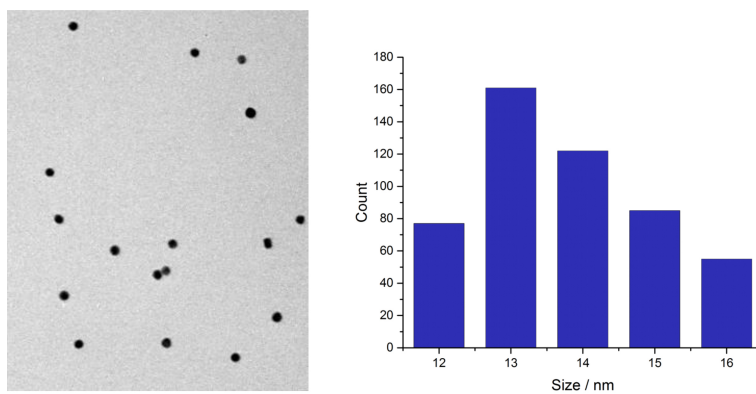


Figure SI-2 – Citrate-stabilised gold nanoparticles used for the construction of the DNA-linked dimer. a) TEM image of 13 ± 2 nm spherical gold nanoparticles. Scale bar is 100 nm. b) Corresponding size distribution histogram, $N = 500$ particles

SI.2 Finite-difference solver for the Mason-Weaver equation

SI.2.1 Dimensionless Mason-Weaver equation

A numerical solver has been designed for the dimensionless version of the Mason-Weaver equation (1). Conversion between the Mason-Weaver equation and its dimensionless form can be achieved using:

$$\zeta = z/z_0 \quad z_0 = \frac{D}{sg} \quad (20)$$

and

$$\tau = t/t_0 \quad t_0 = \frac{D}{s^2 g^2} \quad (21)$$

The aim is now to obtain the time-evolving spatial concentration distribution $c(\zeta, \tau)$ obeying the dimensionless Mason-Weaver equation (22), starting from an arbitrary initial concentration profile $c(\zeta, 0)$.

$$\frac{\partial c}{\partial \tau} = \frac{\partial^2 c}{\partial \zeta^2} + \frac{\partial c}{\partial \zeta} \quad (22)$$

$$\frac{\partial c}{\partial \zeta} + c = 0 \quad @ \zeta = 0, \zeta = \zeta_{\max} \quad (23)$$

A finite-difference scheme for numerically solving this equation has been proposed previously,[17] but unfortunately, in our hands, this did not yield a working computer code. In particular, the proposed time coordinate transformation leads to unsurmountable numerical problems in our implementation. Here, we propose a different finite-difference approximation that yields a stable, robust numerical solver, that moreover does not suffer from mass conservation problems reported[17] for the previously proposed scheme.

SI.2.2 Crank-Nicolson scheme

Time and space are discretised into $N + 1$ and $J + 1$ grid points, respectively. Space is on an evenly spaced grid between 0 and ζ_{\max} .

$$\zeta_j = j\Delta\zeta \quad (j = 0, 1 \dots J) \quad (24)$$

$$\Delta\zeta = \frac{\zeta_{\max}}{J} \quad (25)$$

Time may be on an evenly or unevenly spaced grid. We use an exponentially expanding grid, going from 0 to τ_{\max} .

$$\tau_n = \exp(kn) - 1 \quad (n = 0, 1 \dots N) \quad (26)$$

$$k = \frac{\ln(\tau_{\max} + 1)}{N}$$

We make the following Crank-Nicolson style finite-difference approximations for the PDE, where c_j^n is the value of $c(\zeta_j, \tau_n)$.

$$\frac{\partial c}{\partial \tau} \rightarrow \gamma(c_j^{n+1} - c_j^n) \quad (27)$$

$$\frac{\partial^2 c}{\partial \zeta^2} \rightarrow \alpha(c_{j+1}^n - 2c_j^n + c_{j-1}^n + c_{j+1}^{n+1} - 2c_j^{n+1} + c_{j-1}^{n+1}) \quad (28)$$

$$\frac{\partial c}{\partial \zeta} \rightarrow \beta(c_{j+1}^n - c_{j-1}^n + c_{j+1}^{n+1} - c_{j-1}^{n+1}) \quad (29)$$

where (noting the factors 2 and 4 in α and β)

$$\gamma = \frac{1}{\tau_{n+1} - \tau_n} \quad \alpha = \frac{1}{2(\Delta\zeta)^2} \quad \beta = \frac{1}{4\Delta\zeta} \quad (30)$$

With these finite-difference approximations, and after rearrangement of the terms, the discrete Mason-Weaver equation can be written as follows ($j = 1, 2 \dots J - 1$).

$$\begin{aligned} (-\alpha + \beta)c_{j-1}^{n+1} + (\gamma + 2\alpha)c_j^{n+1} + (-\alpha - \beta)c_{j+1}^{n+1} \\ = (\alpha - \beta)c_{j-1}^n + (\gamma - 2\alpha)c_j^n + (\alpha + \beta)c_{j+1}^n \end{aligned} \quad (31)$$

The boundary conditions are set as follows. At $\zeta = 0$ we choose

$$c \rightarrow \frac{1}{4}(c_0^n + c_0^{n+1} + c_1^n + c_1^{n+1}) \quad (32)$$

$$\frac{\partial c}{\partial \zeta} \rightarrow 2\beta(c_1^n - c_0^n + c_1^{n+1} - c_0^{n+1}) \quad (33)$$

Approximation of c using (32) (instead of simply taking the values at c_0) leads to much better behaviour in terms of mass conservation (the sum over all c_j), in particular at longer times.

After substitution and rearrangement this results in

$$(-2\beta + \frac{1}{4})c_0^{n+1} + (2\beta + \frac{1}{4})c_1^{n+1} = (2\beta - \frac{1}{4})c_0^n + (-2\beta - \frac{1}{4})c_1^n \quad (34)$$

At $\zeta = \zeta_{\max}$ the equivalent choice was made (using backward difference instead of forward difference, naturally).

The equations (discretised PDE and BCs) are assembled into a matrix equation involving tridiagonal matrices. Numerically solving this equation yields the c_j^{n+1} from c_j^n , *i.e.* the concentration profile at time τ_{n+1} using the concentration profile from time τ_n . Repeating the process, starting from the initial condition at τ_0 , yields the evolution of the concentration profile, obeying the Mason-Weaver equation.

SI.2.3 Implementation

The finite-difference scheme was implemented using Python (with `numpy` for array manipulation and sparse matrix routines from `scipy`). For brevity, we only give the solver code without any plotting, processing or storage of results. It consists of a single loop that generates the successive concentration profiles c_j^n at each τ_n , starting from the initial conditions at τ_0 .

```
# -*- coding: utf-8 -*-

import numpy as np
from scipy import sparse
from scipy.sparse import linalg

"""Solver for the adimensional Mason-Weaver equation.

The solution is calculated on an exponentially expanding time
grid (N+1 points), and an evenly spaced space grid (J+1 points).

Input:
    zeta_max (float): adimensional height of the cell
    tau_end (float): calculate solution from tau=0 to tau=tau_end
    J (int): number of space points minus 1 on (linear) grid
    N (int): number of time points minus 1 on (exponential) grid

Output:
    The solution is stored in a two-dimensional array 'c'.
    The space grid points are given by the vector 'zeta'.
    The time grid points are given by the vector 'tau'.

code tested with Python 3.5.2, Anaconda 4.1.1 (64-bit)
"""

def _tridiatrix(J,ldiagelem,cdiagelem,rdiagelem,
               cstart,rstart,lend,cend):
```

```

"""utility function that generates a sparse tridiagonal
matrix from given elements"""
ldiag = np.empty(J+1)
cdiag = np.empty(J+1)
rdiag = np.empty(J+1)
ldiag.fill(ldiagelem)
cdiag.fill(cdiagelem)
rdiag.fill(rdiagelem)
cdiag[0]=cstart
rdiag[1]=rstart
ldiag[-2]=lend
cdiag[-1]=cend
diag=[ldiag,cdiag,rdiag]
N = J+1
return sparse.spdiags(diag,[-1,0,1],N,N,format="csr")

# set calculation parameters
zeta_max = 10. # height of cell
tau_end = 10. # end tau
J = 400 # number of space points (-1)
N = 200 # number of time points (-1)
c_init = np.ones(J+1) # initial condition

# define time and space grids
k_tau = np.log(tau_end+1)/N
tau = -1.0 + np.exp(k_tau*np.arange(0,N+1))
dltzeta = zeta_max/J
zeta=np.linspace(0,zeta_max,J+1,endpoint=True)

# create c array for storing result
c = np.zeros((J+1,N+1))
c[:,0] = c_init

c_n = c_init
dltzeta=dltzeta
tau=tau
# loop generating  $c^{n+1}$  from  $c^n$  starting from  $c^0$ 
for n in range(0,N):
    alpha = 1/(2*(dltzeta**2))
    beta = 1/(4*dltzeta)
    gamma = 1/(tau[n+1]-tau[n])

    # finite difference diagonals Left Hand Side
    ldiagelem = -alpha + beta
    cdiagelem = gamma + 2*alpha
    rdiagelem = -alpha - beta
    # boundary conditions LHS
    cstart = -2*beta + 0.25
    rstart = 2*beta + 0.25

```

```

lend = -2*beta + 0.25
cend = 2*beta + 0.25
# create LHS tridiagonal matrix
LHSmat = _tridiamatrix(J,ldiagelem,cdiagelem,rdiagelem,
                        cstart,rstart,lend,cend)

# finite difference diagonals Right Hand Side
ldiagelem = alpha - beta
cdiagelem = gamma - 2*alpha
rdiagelem = alpha + beta
# boundary conditions RHS
cstart = 2*beta - 0.25
rstart = -2*beta - 0.25
lend = 2*beta - 0.25
cend = -2*beta - 0.25
# create RHS tridiagonal matrix
RHSmat = _tridiamatrix(J,ldiagelem,cdiagelem,rdiagelem,
                        cstart,rstart,lend,cend)
# construct RHS vector
RHSvec = RHSmat * c_n # c contains concentration profile

# SOLVE the matrix equation, giving c^{n+1} (c_next)
c_next = linalg.spsolve(LHSmat,RHSvec)
# store c_{n+1} into solution matrix
c[:,n+1] = c_next

# we swap the vectors containing c_n and c_next via cswap
# we cannot simply re-assign c_n = c_next
cswap = c_n
c_n = c_next
c_next = cswap

# plot example
import matplotlib.pyplot as plt

plt.figure(1)
plt.clf()
for i in [0,50,100,150,200]:
    plt.plot(zeta, c[:,i],label='tau='+str(tau[i]))
plt.ylim(0,3)
plt.xlabel('$\\zeta$')
plt.ylabel('$c$')
plt.legend()
plt.show()

```

SI.2.4 Validation of the numerical solution

The numerical solver was tested extensively for a wide range of ζ_{\max} and τ . Typical values for N and J were on the order of several hundred grid points. Numerical mass conservation and convergence of the gradient to the analytical Boltzmann equilibrium solution were verified.

An example of a numerical solution is given in Figure SI-3, which also illustrates that the numerical solution faithfully converges to the analytical equilibrium distribution, for $\tau = 1.4\tau_{\text{sed}}$.

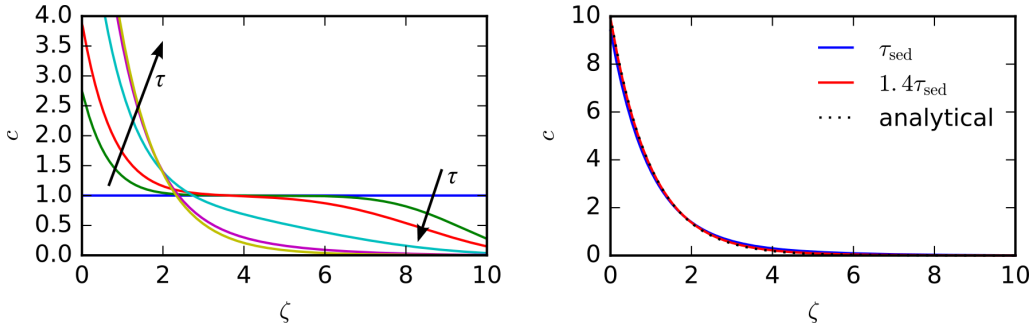


Figure SI-3 – Left: Numerical solution ($N = 200$, $J = 400$) to the dimensionless Mason-Weaver equation with $\zeta_{\max} = 10$ and τ going from 0 to 30. Right: Comparison of the analytical equilibrium profile and the numerical solution at longer times, demonstrating (1) that the numerical solution converges to the analytical equilibrium (Boltzmann) distribution and (2) that at $1.4\tau_{\text{sed}}$ the system is virtually at equilibrium.

Mass conservation is observed in the numerical scheme, as illustrated in Figure SI-4. A slight increase of the total numerical mass is observed, but the numerical solution does not diverge at longer simulation times, thanks to the choice for setting the boundary conditions, *cf.* Equation (32).

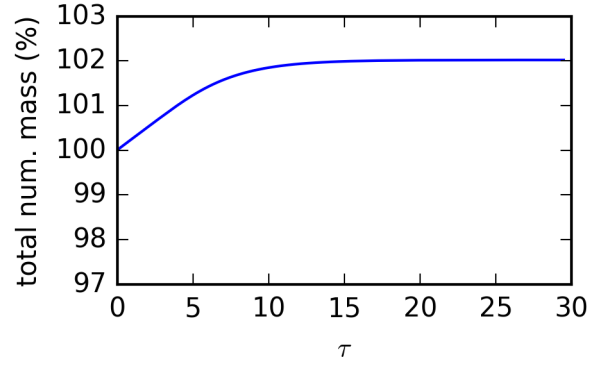


Figure SI-4 – Evolution of the total mass in the numerically simulated system ($N = 200$, $J = 400$, $\zeta_{\max} = 10$, $\tau = 0 \dots 30$), obtained by summing all space grid points. A slight increase ($< 2\%$) of the total numerical mass is observed, but the total mass does not diverge for long simulation times.

SI.3 Sedimentation parameters for gold nanospheres

Table SI-2 – Calculated diffusion D and sedimentation s coefficients for gold nanoparticles in water at two different temperatures.

diam. (nm)	298 K		277 K	
	0.89 mPa.s		1.56 mPa.s	
	D $10^{-12} \text{ m}^2\text{s}^{-1}$	s 10^{-9} s	D $10^{-12} \text{ m}^2\text{s}^{-1}$	s 10^{-9} s
13	37.8	0.204	19.9	0.116
20	24.5	0.482	13.0	0.274
40	12.3	1.93	6.48	1.10
50	9.82	3.01	5.18	1.71
60	8.18	4.34	4.32	2.47
80	6.14	7.72	3.24	4.38
100	4.91	12.1	2.59	6.85
150	3.27	27.1	1.73	15.4

Table SI-3 – Values of equilibrium gradient length scale z_0 (in mm) for spherical gold nanoparticles in water, at two different temperatures (room temperature and fridge)

diam. (nm)	z_0 (mm)	
	298 K	277 K
13	18.886	17.556
20	5.187	4.821
40	0.648	0.603
50	0.332	0.309
60	0.192	0.179
80	0.081	0.075
100	0.041	0.039
150	0.012	0.011

Table SI-4 – Calculated concentration factor B for spherical gold nanoparticles in water at 277K (left columns) and 298K (right columns), for cell heights (z_{\max}) of 1 mm and 1 cm

diam. (nm)	277K		298K	
	B			
	1 mm	1 cm	1 mm	1 cm
13	1.03	1.31	1.03	1.29
20	1.11	2.37	1.10	2.26
40	2.05	16.6	1.96	15.4
50	3.24	33.7	3.01	31.7
60	5.62	56.0	5.23	52.1
80	13.3	133	12.3	123
100	25.9	259	24.1	241
150	87.5	875	81.3	813

Table SI-5 – Calculated sedimentation times (in hours) for gold nanoparticles in water for a cell with $z_{\max} = 1$ cm. Time to reach equilibrium is $t_{\text{equil}} \approx 1.4t_{\text{sed}}$. These times are directly proportional to cell height.

diam. (nm)	$t_{\text{sed}}(h)$	
	298 K	277 K
13	1390	2450
20	587	1030
40	147	258
50	93.9	165
60	65.2	115
80	36.7	64.6
100	23.5	41.3
150	10.4	18.4

SI.4 Experimental test of the centrifugation parameters recommended by the Mason-Weaver model

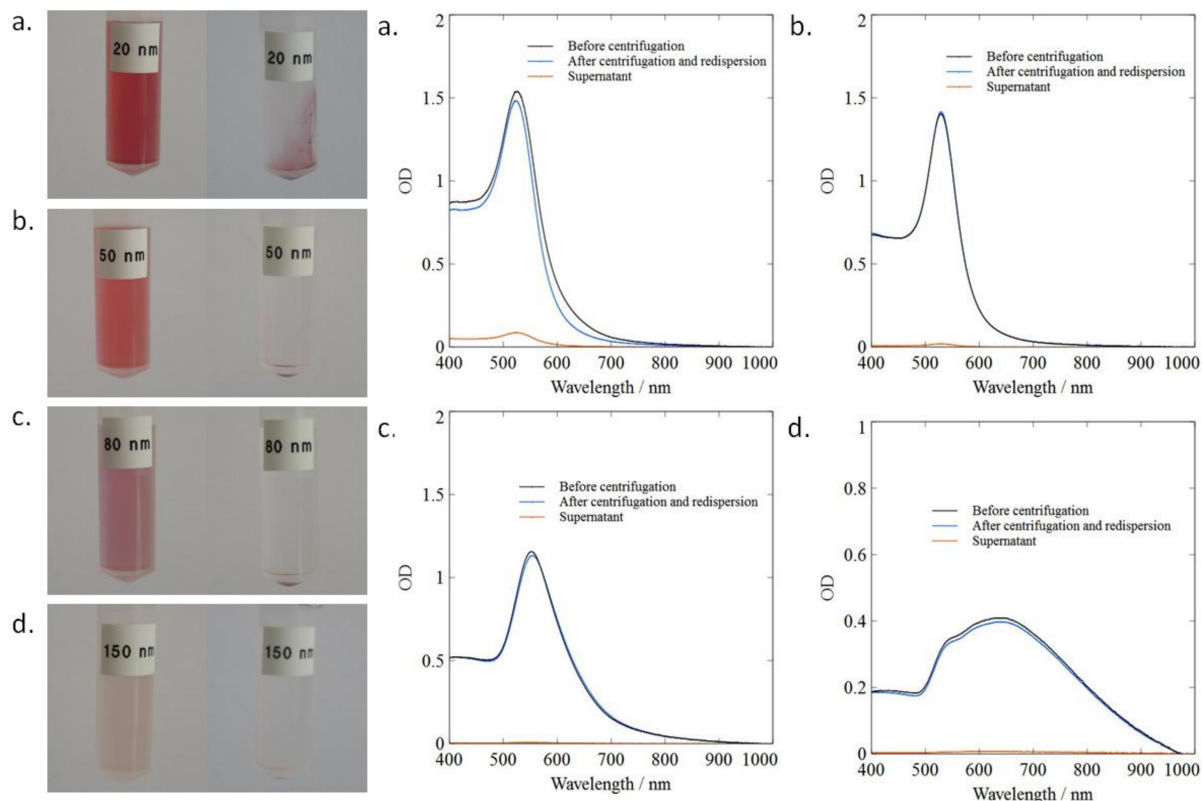
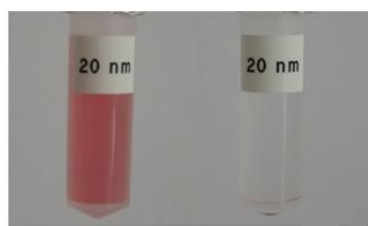


Figure SI-5 – Centrifugation of gold nanospheres in water, for 30 minutes at the centrifugal acceleration recommended by the Mason-Weaver model. Diameters: (a) 20 nm, (b) 50 nm, (c) 80 nm, (d) 150 nm. Photographs on the left: centrifuge vials before and after centrifugation. Relative centrifugal force: (a) $4931 \times g$, (b) $789 \times g$, (c) $308 \times g$, (d) $88 \times g$. UV-visible extinction spectra on the right: sample before centrifugation (black) and after (blue) re-dispersion of the liquid pellet (5% of the initial volume); red: supernatant (95% of the initial volume).

a.



b.

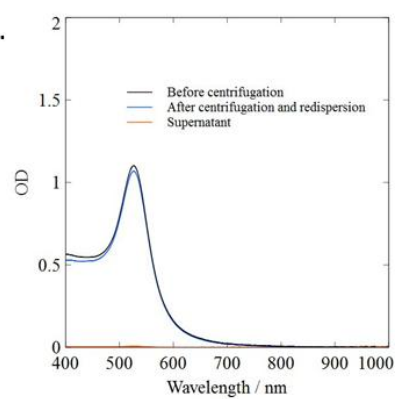


Figure SI-6 – Centrifugation of 20 nm diameter gold nanospheres in water, for 30 minutes, at $6000 \times g$, *i.e.* 20% higher than the Mason-Weaver recommendation.